Geophysical Research Letters

RESEARCH LETTER
10.1029/2018GL081471

Imaging Subduction Beneath Mount St. Helens: Implications for Slab Dehydration and Magma Transport

Michael Everett Mann[1], Geoffrey A. Abers[1], Kayla Crosbie[1], Kenneth Creager[2], Carl Ulberg[2], Seth Moran[3], and Stéphane Rondenay[4]

[1]Department of Earth and Atmospheric Sciences, Cornell University, Ithaca, NY, USA, [2]Department of Earth and Space Sciences, University of Washington, Seattle, WA, USA, [3]Cascades Volcano Observatory, United States Geological Survey, Vancouver, WA, USA, [4]Department of Earth Science, University of Bergen, Bergen, Norway

Key Points:
- The Juan de Fuca slab is imaged at 68 km without tears beneath Mount St. Helens, extremely shallow for a slab beneath an arc volcano
- Continental Moho signals disappear in the forearc due to both high lower-crustal velocities and hydration of the mantle wedge
- Magma must migrate laterally from further in the back arc or along strike to supply Mount St. Helens and surrounding forearc volcanic vents

Supporting Information:
- Supporting Information S1

Correspondence to:
M. E. Mann,
mem533@cornell.edu

Citation:
Mann, M. E., Abers, G. A., Crosbie, K., Creager, K., Ulberg, C., Moran, S., & Rondenay, S. (2019). Imaging subduction beneath Mount St. Helens: Implications for slab dehydration and magma transport. *Geophysical Research Letters*, *46*, 3163–3171. https://doi.org/10.1029/2018GL081471

Received 27 NOV 2018
Accepted 28 FEB 2019
Accepted article online 4 MAR 2019
Published online 21 MAR 2019

Abstract Mount St. Helens (MSH) is anomalously 35–50 km trenchward of the main Cascade arc. To elucidate the source of this anomalous forearc volcanism, the teleseismic-scattered wavefield is used to image beneath MSH with a dense broadband seismic array. Two-dimensional migration shows the subducting Juan de Fuca crust to at least 80-km depth, with its surface only 68 ± 2 km deep beneath MSH. Migration and three-dimensional stacking reveal a clear upper-plate Moho east of MSH that disappears west of it. This disappearance is a result of both hydration of the mantle wedge and a westward change in overlying crust. Migration images also show that the subducting plate continues without break along strike. Combined with low temperatures inferred for the mantle wedge, this geometry greatly limits possible source regions for mantle melts that contribute to MSH magmas and requires lateral migration over large distances.

Plain Language Summary Subducting oceanic plates are heated as they descend into the Earth and release fluids, generating magma that feeds overlying arc volcanoes. As a result, volcanic arcs occur along lines above where the subducting plates reach a characteristic depth, typically 100 km beneath them. The location of Mount St. Helens (MSH) volcano 35–50 km in front of the main arc of volcanoes in Cascadia is puzzling and an anomaly globally. We provide the first clear image of the subducting oceanic plate beneath MSH and find it to be 68 ± 2 km deep, making this the shallowest directly imaged subducting plate beneath an arc volcano anywhere. This suggests an unusual magma pathway. The base of the North American crust, or Moho, disappears immediately to the west of MSH, indicating a close relationship between volcano location and geological processes. The geometry creates a problem in that mantle temperatures should be too low to generate magma in the mantle beneath MSH, yet the volcano occasionally erupts magmas generated in the mantle. These observations provide some of the best evidence anywhere for lateral as well as vertical transport of magma from the mantle to volcanic arcs.

1. Introduction

Subduction zone volcanoes form arcs parallel to slab strike where the subducting plate reaches depths of ~100 km, with this characteristic depth varying from region to region (e.g., England et al., 2004; Syracuse & Abers, 2006). At these depths, the slab has passed beneath a cold forearc and into a mantle wedge environment hot enough to produce arc basalts (e.g., Syracuse et al., 2010). Within this hot subarc region, fluids and melt ascend from the slab to arc volcanoes on paths that are often assumed to be vertical (e.g., Grove et al., 2012) but are likely deflected downward by solid flow (Cagnioncle et al., 2007) and channeled updip in compaction-mediated permeability pathways (Wilson et al., 2014). Overall, it is often assumed that the volcanic front location reflects the trenchward extent of high temperatures in the wedge (England & Wilkins, 2004).

The Mount St. Helens (MSH) volcano is located 35-50-km west of the main Cascade arc defined locally by Mount Adams (Figure 1; Hansen et al., 2016). In addition to its main edifice, nearly 150 Quaternary basaltic volcanic vents extend east and south from MSH to the Columbia River, with a few vents lying even further west (Evarts et al., 2009; Hildreth, 2007). Regional slab models extrapolate geometry for hundreds of kilometers due to the absence of Wadati-Benioff zone (WBZ) seismicity between 41°N and 47°N and suggest

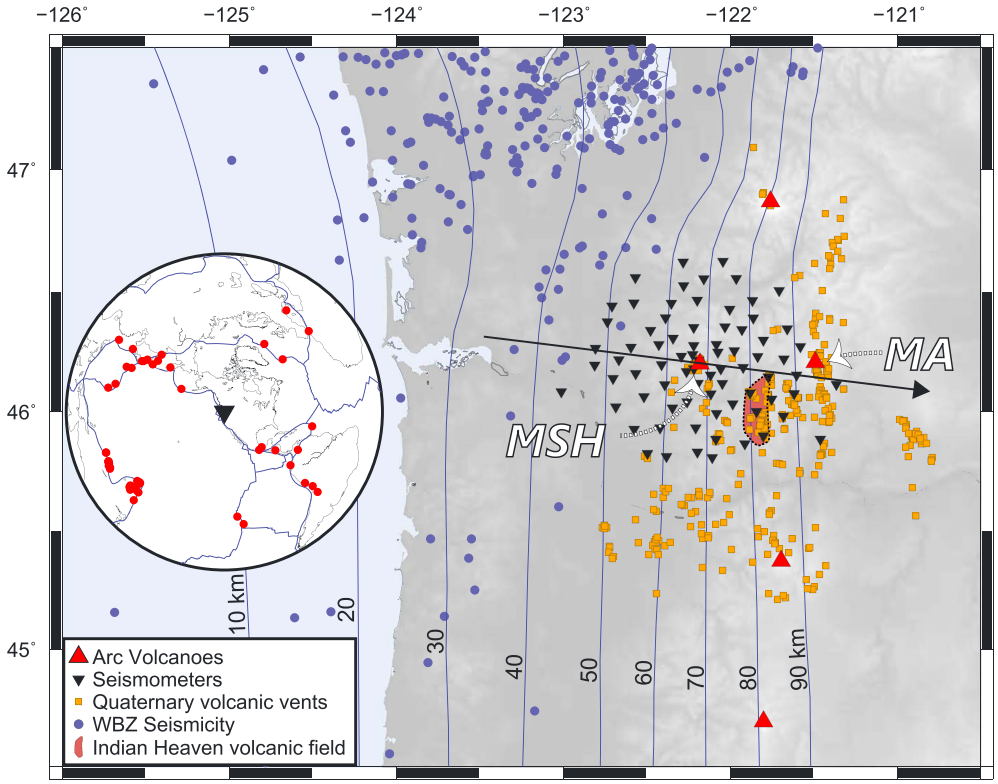

Figure 1. Cascadia subduction zone and seismic network. Slab contours from McCrory et al. (2012). (inset) Distribution of earthquakes analyzed. MSH = Mount St. Helens; MA = Mount Adams; maroon = Indian Heaven volcanic field (Hildreth, 2007); black arrow = dip direction of Juan de Fuca plate.

slab depths of 65–70 km under MSH (McCrory et al., 2012). These depths are unusually shallow compared with other arc volcanoes globally (Syracuse & Abers, 2006) and are shallower than for all other Cascade arc volcanoes. This unusual geometry may be due to an error in the slab geometry models, or it may be a consequence of a nearby hole or tear in the subducting Juan de Fuca (JdF) slab that allows melt in the shallow mantle wedge, an idea supported by teleseismic arrival time tomography (e.g., Darold & Humphreys, 2013; Michaelson & Weaver, 1986). By contrast, the forearc Moho is absent in much of the region, leading to interpretations of widespread serpentinization of the shallow forearc that require mantle temperatures too cold to allow melting (Bostock et al., 2002; Brocher et al., 2003), extending to the edifice at MSH. To explain this contradiction, Hansen et al. (2016) proposed that melt migrates laterally from the backarc.

To distinguish between these possibilities for arc geometry, we image the subduction system beneath MSH using receiver function (RF) methods from a dense array of broadband seismometers. Strong signals show that the subducting JdF crust is continuous without holes or tears and is anomalously shallow beneath MSH. We also delineate the sharp change in the upper-plate Moho from east to west of MSH. While lateral melt transport remains the most likely explanation for the forearc volcanism, it remains unclear where these pathways are or why this phenomenon occurs in part of the Cascade arc and not elsewhere either in the Cascades or globally.

2. Data and Preprocessing

The imaging Magma Under MSH (iMUSH) broadband experiment deployed 70 seismometers at ~10-km spacing within 50 km of MSH (Figure 1), from June 2014 to August 2016. Unlike most previous linear broadband arrays in subduction zones (e.g., see review in Bostock, 2013), the iMUSH array was distributed to allow three-dimensional (3-D) imaging, with crossing rays to at least 100-km depth. We analyze the *P* coda for teleseismic arrivals, initially for all 269 earthquakes with visible signals between 30° and 90° distance with

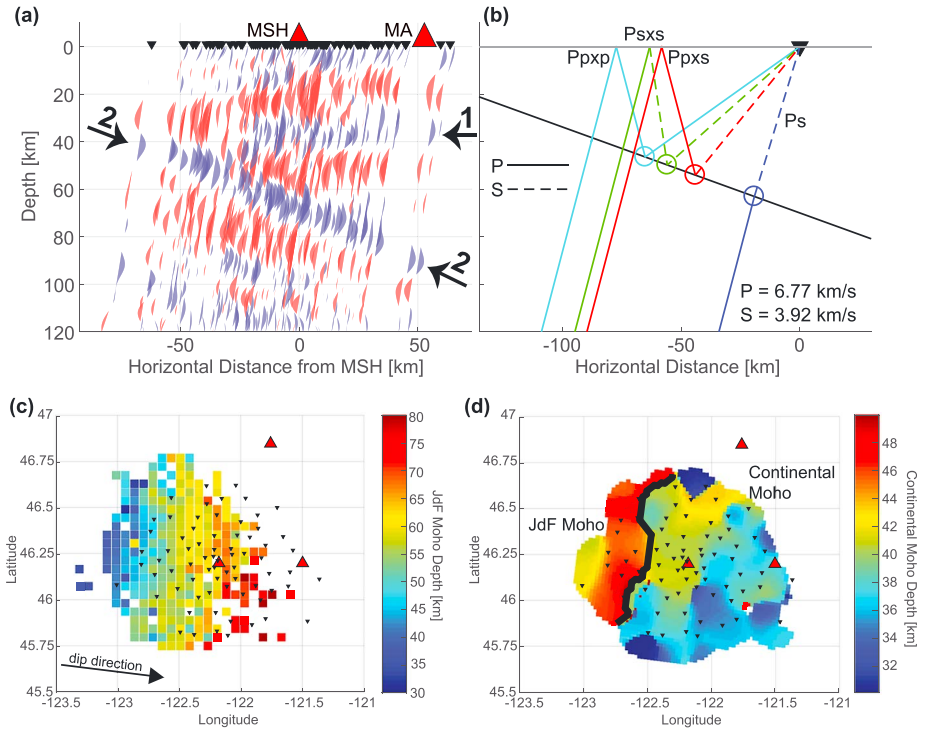

Figure 2. (a) Receiver function back-projection from one earthquake at 244° back azimuth. Blue peaks are positive; red are negative. Each trace is normalized to peak amplitude. (1) Subhorizontal continental Moho signals. (2) Dipping JdF Moho signals. (b) Ray nomenclature and paths calculated for different phases. Circles along dipping interface represent conversion/reflection points. (c) Averaged conversion points from picked Ppxs peaks after back-projection; see text. (d) Depth of continental Moho from Common-Conversion-Point stack of both the Ppxs and Psxs phases. Red triangles = arc volcanoes; inverted black triangles = seismometers. MSH = Mount St. Helens; MA = Mount Adams; JdF = Juan de Fuca.

MW > 5.5 recorded by the iMUSH array, supplemented with six nearby broadband stations (Figure 1). Each three-component seismogram is decimated to 10 samples per second and band-pass filtered between 0.03 and 1 Hz using a zero-phase second-order Butterworth filter. The first 90 s of the *P* wavetrain is used to estimate the teleseismic-scattered *P* wavefield using an array-based deconvolution procedure (Bostock & Rondenay, 1999; Pearce et al., 2012). We refer to the resulting time series as RFs despite some differences with traditional RFs, most notably the lack of a zero-lag peak due to transformation into *P-SV* polarization prior to deconvolution (Rondenay, 2009).

We generate array-based RFs for each of the 269 earthquakes and examine them for coherency (Figures 2a and 2b). First, data are low-pass filtered at 0.2 Hz to better isolate coherent phases such as slab conversions. These event gathers are visually inspected, retaining only signals where coherent phases could be visually identified. To better visualize the structures responsible for those phases, we plot them with depth in a reference 1-D velocity model (e.g., Figures 2a and 2b), assuming that dominant conversions are the Ppxs phase (free-surface-reflected *P* converting to *S* at the scatterer; Figure 2b) due to its high-depth resolution (Rondenay, 2009) and low noise (Pearce et al., 2012). The back-projections use a reference 1-D *S* velocity model derived from an inversion of surface waves from ambient noise and earthquakes (supporting information Figure S1; Crosbie, 2018), estimating crustal Vp/Vs and density in the upper 40 km from Brocher (2005) and mantle Vp/Vs of 1.75. These analyses result in 61 earthquakes after eliminating earthquakes producing ringy or inconsistent RFs. Of the 71 stations with usable data, we retain an average of 43 RFs per event and 2,652 RFs in total after removing individual RFs that show anomalous amplitudes, long-period drift, or near-monochromatic ringing.

Five stations had measured orientation problems; four stations were misoriented by 15–17° and one by 180°. Inspection of transverse-component RFs confirmed these corrections; however, these stations did not produce usable RFs.

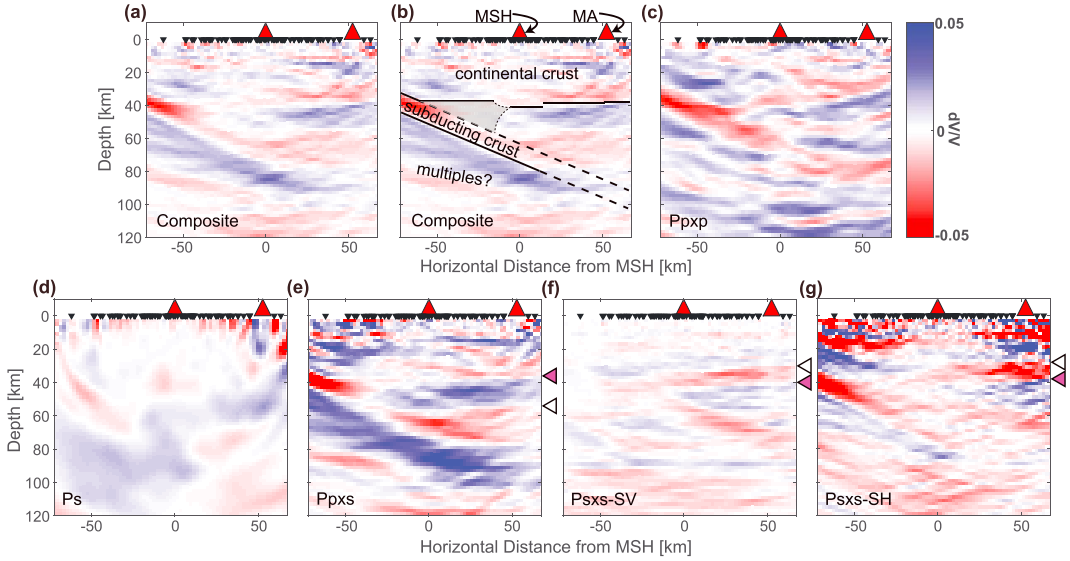

Figure 3. (a) Composite *S* migration image. (b) Interpreted *S* migration image, boundaries dashed where inferred. Gray polygon = potentially hydrated mantle wedge. (c–g) Individual-phase *S* migration images, as labeled. Black inverted triangle = seismometers; red triangle = Cascade Arc volcanoes; MA = Mount Adams; MSH = Mount St. Helens; purple triangles = interpreted continental Moho; white triangles = ghost Mohos.

3. Methods

3.1. Back-Projection

The 61 RF sets are analyzed by means of two back-projection analyses. First, we select peaks in the RFs we believe are associated with the subducting JdF plate and back-project them to depth while explicitly accounting for 3-D ray bending from a planar dipping interface (Supporting Information S1; Richards et al., 1991). Rays are traced through a uniform-velocity mantle wedge with an identical average slowness as in the 1-D velocity model used in the migration (Figure 2b), while an underlying dipping interface generates conversion-point locations (Figure 2b). This analysis allows for areal mapping of the slab interface, correcting for the dip artifacts that are present in simpler back-projections (e.g., Figure 2a). In the second analysis, the RF signals form the basis of 3-D Common-Conversion-Point (CCP) stacking (e.g., Dueker & Sheehan, 1997) to image the upper-plate Moho, discussed below.

3.2. Migration

The scattered wavefield is migrated with a 2-D generalized Radon transform method that utilizes ray theory and assumes single scattering (Figure 3), using a process fully described elsewhere (Bostock et al., 2001; Rondenay, 2009). We invert the scattered wavefield for 2-D *P* and *S* wave velocity perturbations necessary to produce the scattering in the plane normal to slab strike. The migration method is best at constraining gradients in these velocity perturbations. The same 61 earthquakes used in our back-projection analyses are used in the migration, after band-pass filtering 0.03 to 0.6 Hz. The *P* wave velocity perturbations are generated from the surface-reflected *P* scattered wavefield (Ppxp; Figure 3c), and the *S* wave velocity perturbations are generated from several forward-scattered and primary surface-reflected conversions (Figures 2b and 3a–3f). Because the surface-reflected conversions have superior depth resolution relative to the forward-scattered conversions, they are weighted higher than Ps (Pearce et al., 2012), with weights of 0.1 for Ps, 1 for Ppxs, 0.5 for Psxs-SH, and 0.25 for Psxs-SV.

4. Results

4.1. Slab Discontinuity Geometry

The RFs show a strong converter dipping eastward, related to the subducting JdF plate (Figure S3a). It resembles features seen in similar data sets (Abers et al., 2009; Nicholson et al., 2005; Rondenay et al., 2001), and its polarity indicates increasing velocity with depth. We infer that this is the Moho in the JdF

plate. The RFs also reveal a subhorizontal interface near 35–40-km depth in several phases, which appears to be the upper-plate Moho. Because of the consistency and resolution of the JdF Ppxs phase, we use it to map the subducting plate throughout the area. Specifically, we pick lag times from 1,514 positive-polarity peaks identified by hand on back-projections of individual earthquakes. Peaks are picked as the highest positive amplitude within a 20-km vertically thick window manually defined around these projected peaks (e.g., Figure 2a). This method generates some artifacts, particularly in the western region where it is difficult to separate the subducting JdF Moho from the upper-plate Moho or from complexities sometimes seen in the nose of the mantle wedge. However, this procedure captures the slab interface sufficiently to determine its geometry.

The conversion points inferred from the individual RF peaks are then fit to a 2-D polynomial describing the converter depth, after the dip-corrected back-projection described above, iteratively adjusting the strike and dip used in the back-projection to fit observed lag times. We iterate the fitting process until strike and dip converge at <0.01° change. An *F* test shows that a plane fits the data as well as any higher-order surface. The resulting strike, dip, and depth of the JdF Moho are 7.0 ± 2.6° clockwise from North, 19.8 ± 0.6°, and 70.0 ± 0.6 km directly beneath MSH, respectively (uncertainties represent 95% confidence interval).

Once the strike and dip are established, all rays are retraced to the converter. The converting interface is then mapped by averaging the back-projected conversion points in horizontal 5 km × 5 km bins (Figure 2c). This 3-D imaging procedure yields two important results. First, it shows that the mapped interface is continuous along-strike beneath this array. Second, this map illustrates that the coverage of the subducting slab is complete in the along-strike span of the array but displaced updip from the stations.

4.2. CCP Stacking for Upper Plate Moho

To better image the upper-plate Moho in 3-D, we use a CCP stacking method that back-projects RFs to depth in three dimensions in the 1-D reference velocity model. CCP volumes are stacked separately for Ps, Ppxs, and Psxs phases (Figure S4), and the reverberated phases are stacked together (Figure S5). Details regarding the CCP stacking method are described in Supporting Information S1. Because CCP stacking assumes flat-lying layers, conversions from the dipping JdF Moho decorrelate and are not interpreted here.

The continental Moho is mapped as the maximum amplitude between 30- and 50-km depth within nodes that include more than six measurements. These amplitudes are identified and mapped in each individual-phase CCP stack (Figure S7), as well as in the reverberated-phase CCP stack. Peak amplitudes and depths of the continental Moho are determined by fitting a Gaussian function to each vertical column of the stacked CCP volume in this depth range. The peaks appear more consistent in the reverberated phases than in the direct Ps phase (Figure S7), as with 2-D migration (Figure 3d). Consequently, we interpret the continental Moho in the Ppxs phase.

The continental Moho signal disappears 15-km west of MSH in our CCP stacking image, and farther west, this procedure picks up the JdF Moho (Figure 2d). We define the westward extent of the continental Moho as the point at which our procedure begins to pick the JdF Moho and has reduced amplitude (Figure 2d). The continental crust is thicker to the north of MSH (40–44 km) than to the south, with the thinnest crust (34 km) found 15-km south-southeast of MSH beneath the Indian Heaven volcanic field.

4.3. Two-Dimensional Migration Images

Unlike the back-projection method, the migration method makes no assumptions concerning conversion geometry other than two-dimensionality of structure, a simple 1-D background velocity model, and single scattering (Rondenay, 2009). We migrate the RF waveforms as described above, assuming the strike of 2-D structure determined from back-projection (7.0°). The *P* migration image (Figure 3c) has lower resolution than the composite *S* migration image (Figures 3a and 3b) but shows a similar overall structure.

Robust features in the composite S image ideally appear in each individual phase, but some potential artifacts appear. A subhorizontal velocity inversion (i.e., a fast layer over a slow layer) at 55-km depth appears in the mantle wedge of the Ppxs image (Figure 3e), which is the only individual-phase image in which this boundary occurs. This velocity inversion exhibits the exact timing as the upper-plate Moho in Psxs, which for flat interfaces can appear in the Ppxs image due to similarity of moveout and small ray parameter range. It is likely a ghost image of that Psxs Moho, with reversed polarity due to the differing behavior of these two

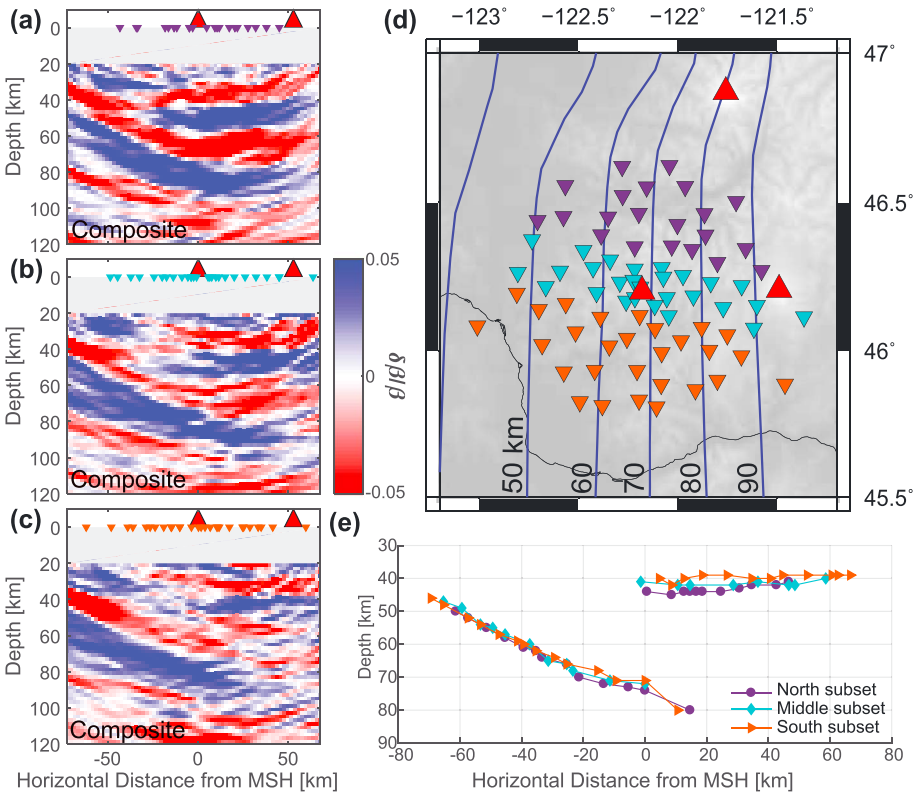

Figure 4. (a) Migration for northern subset of the array, (b) middle subset, and (c) southern subset. All migration images are composite *S* images as Figure 3a. (d) Subset station locations, denoted by color. Blue lines = slab contours (McCrory et al., 2012). (e) Continental and Juan de Fuca Moho locations for the three migration subsets, picked where Vs perturbations cross from negative above to positive below.

signals. This likely ghost signal persists as a subhorizontal velocity inversion in the composite S image. It could be incorrectly interpreted as, for example, the base of the lithosphere. Similarly, the velocity inversion seen at 30-km depth in the Psxs images is most likely a ghost generated by the Moho in Ppxs (Figures 3f and 3g). For these reasons, interpretation focuses on features that appear consistently in multiple phases.

The composite *S* image (Figures 3a and 3b) shows a low-velocity layer between 32- and 43-km depth at the west edge of the image dipping eastward; we interpret this as the subducting JdF crust. It resembles that seen elsewhere along strike (e.g., Abers et al., 2009; Audet et al., 2010; Bostock et al., 2002). It is difficult to determine if the top of the JdF crust disappears below 40-km depth or simply decreases in *S* velocity contrast with the overlying mantle to noise levels. A dipping positive discontinuity (slow over fast), interpreted as the JdF Moho, persists to at least 80-km depth, beyond which resolution degrades (Figure 2c). The resulting depth of the JdF Moho beneath MSH is 74 km, placing the slab surface at 68 km beneath MSH assuming a JdF crustal thickness of 6 km as seen offshore (Han et al., 2016). The 4-km-depth discrepancy between the migration and the 70-km Moho depth determined from back-projection (Figure 2c) is due to several factors, primarily the use of a constant velocity model in the back-projection. The depth of 74 km from the migration is preferred for these reasons. The continental Moho is well defined as a positive interface near MSH at 40 ± 1-km depth and near Mount Adams at 37 ± 1-km depth.

The main feature of the *P* wave migration image is the eastward-dipping low-velocity JdF crust (Figure 3c) that continues to at least 60-km depth. It provides independent confirmation of the JdF Moho mapped from *S* wave conversions. Other features of the *P* migration image are not interpreted here because it has a lower resolution than the *S* migration images.

Although a full 3-D migration of this data set is beyond the scope of this study, the data are divided into three independent station groups at different across-strike corridors and migrated separately within each group

(Figures 4a–4c). Each migration shows a dipping JdF Moho at approximately the same location and a well-defined continental Moho east of MSH, with slightly shallower continental Moho depths to the south (Figure 4e) consistent with our CCP stacking (Figure 2d). These results indicate a planar slab surface with no obvious variation along-strike, whereas there is an 8–10-km variation in topography of the upper-plate Moho.

The small variability in JdF Moho location between the three independent migrations (Figure 4) provides an indication of uncertainty in slab depth due to noise in the migration procedure and to the assumption of two-dimensionality. The root-mean-square (RMS) variation in depth between the three sections is $\leq$1 km (Figure 4e) between 49- and 72-km depth. We estimate an additional 2-km uncertainty due to the assumed velocity model, taken here as the RMS variation in travel time through the 3-D model of Crosbie (2018). This gives an aggregate uncertainty in slab depth of 2 km.

5. Discussion and Conclusions

5.1. Slab Geometry and JdF Moho

The top of the subducting JdF crust is inferred to be 68 $\pm$ 2 km beneath MSH (Figure 3a), making this the shallowest directly imaged subducting crust beneath an arc volcano to date; arc volcanoes with shallower subducting slabs either lie at the edges of slabs where geometry is poorly resolved or in regions without imaging that have poor slab depth constraints (Syracuse & Abers, 2006). The depth determined from our migration results is within 2–3 km of the hand-contoured subduction model of McCrory et al. (2012; Figure 1). Although our ray coverage is weak directly beneath Mount Adams due to ray bending, the JdF Moho extrapolates to a depth of 100 km beneath it, consistent with 94-km depth for the top of the JdF crust, which is slightly deeper than beneath other Cascade arc volcanoes (McCrory et al., 2012) but consistent with global averages (England et al., 2004; Syracuse & Abers, 2006).

The persistence of the JdF Moho to depths greater than 60 km is difficult to reconcile with petrologic models that predict the velocity contrast at the JdF Moho should disappear once the subducting crust eclogitizes by 60-km depth (Rondenay et al., 2008; van Keken et al., 2011, 2018). Similar seismic analyses in Cascadia show a noticeably weaker putative JdF Moho than what we find beneath MSH (Abers et al., 2009; Bostock et al., 2002; Nicholson et al., 2005). Potential explanations for the persistence of the boundary to greater depths include the JdF crust persisting metastably as gabbro or the boundary being produced by the base of a hydrated peridotite layer below the Moho rather than the Moho (Rondenay et al., 2008). The latter interpretation implies that a significant amount of H_2O is being subducted to subarc depths, consistent with evidence for elevated H_2O in Cascade arc magmas (Ruscitto et al., 2010). It is not clear if the stronger Moho here is due to a large iMUSH data set or a peculiarity of the MSH region.

5.2. The North American Plate

Absence of the continental Moho in the forearc has been seen in other migration images in Cascadia and is typically attributed to serpentinization of the cold mantle forearc wedge (e.g., Bostock et al., 2002). A sharp decrease in Moho *P* wave reflectivity immediately to the west of MSH has also been attributed to hydration of the mantle wedge (Brocher et al., 2003; Hansen et al., 2016). However, it is difficult to reconcile the abrupt disappearance of the continental Moho within 10–20 km of MSH with the notion that it is entirely controlled by mantle hydration. Antigorite, the likely serpentine species, lowers the velocity of peridotite much less than older lizardite-based calculations so cannot account for the Moho's complete disappearance (Reynard, 2013). Hydrous phases such as serpentine and chlorite should be stable in the mantle wedge only at <800 °C (reviewed in Abers et al., 2017), whereas MSH dacites equilibrated at 925–940 °C in the lower crust (Blatter et al., 2017). In addition, the presence of Quaternary mantle-sourced basalts at MSH and proximal vents (Hildreth, 2007) indicates temperatures potentially approaching 1,460 °C (Leeman et al., 2005), although H_2O may reduce this estimate by 100–200 °C (Lee et al., 2009).

Observations from ambient-noise tomography (Crosbie, 2018) and regional *P* wave tomography (Parsons et al., 1999) suggest an alternative effect—lower-crustal velocities are 10–15% higher west of MSH than east of it, reducing the Moho velocity contrast. Anomalously high velocities likely result from the gabbroic Siletz terrane forming the basement west of MSH (Wells et al., 2014). Hence, in contrast to previous

interpretations, we infer that lower crustal composition contributes to the change in Moho character in the Cascadia forearc, perhaps equally to mantle hydration.

5.3. Slab Continuity and the Search for Magma Origins

These observations further complicate the search for the origin of MSH and nearby magmas. One possibility is that high-temperature basalts originate from below the young JdF plate through a hole or tear in the slab (Leeman et al., 2005; Weaver & Michaelson, 1985). The continuous signals from the JdF Moho preclude any such hole or tear in the area of the array, and similar observations immediately north (Abers et al., 2009; McGary et al., 2014) indicate this continuity extends northward along-strike. Back-projection supports this assertion (Figure 2c), as do the three migrations using independent data sets (Figures 4a–4c), all of which show a coherent JdF slab along-strike. It is possible that a hole exists south of the array, for example, beneath the Boring volcanics 50 km to the south (Hildreth, 2007), in which case magmas would be required to migrate northward more than 50 km.

Features smaller than the Fresnel-zone diameter cannot be imaged using our techniques, but that diameter is small. For reflected phases like Psxs, the Fresnel-zone diameter is approximately $\sqrt{\left(2z\beta T + T^2\beta^2/4\right)}$, where z is the depth to the interface, β is the S wave velocity, and T is the shortest period (Ryberg & Weber, 2000). For $\beta = 4.0$ km/s and $T = 1$ s, this diameter is 25 km at 75-km depth, limiting possible holes to smaller than 25 km. Although we have not modeled processes creating slab holes, it seems reasonable that holes smaller in diameter than ~40 km (the thermal boundary layer thickness for a 10-Ma plate) are geodynamically implausible.

Alternatively, the forearc magma may originate farther into the backarc (Bedrosian et al., 2018). The Quaternary basaltic vents occur at the latitude of the ~17-Ma Columbia River flood basalts (Camp & Ross, 2004), which, although originating much farther east, represent a significant thermal perturbation to the subduction system that could still be disrupting the slab at greater depth (Obrebski et al., 2010). Numerous Quaternary vents form a 150-km-long cross-arc trend at this latitude (Leeman et al., 2005), indicating unusual magma generation and transport. A substantial and unusual amount of lateral magmatic transport must occur to explain the location of MSH; it is difficult to identify another major volcanic center worldwide that is displaced this far from the arc.

Acknowledgments
We thank O. Bachmann, P. Bedrosian, E. Bowles-Martinez, R. Denlinger, S. Hansen, E. Kiser, A. Levander, V. Salters, B. Schmandt, A. Schultz, and T. Sisson for helpful discussions throughout this project. Comments by E. Humphreys and an anonymous reviewer greatly improved the manuscript. Data collection was supported by the IRIS-PASSCAL Instrument Center, an NSF-supported facility, and the efforts of the entire iMUSH field team. All seismograms provided by the IRIS Data Management Center. This work was funded by NSF grant EAR-1444275.

References

Abers, G. A., MacKenzie, L. S., Rondenay, S., Zhang, Z., Wech, A. G., & Creager, K. C. (2009). Imaging the source region of Cascadia tremor and intermediate-depth earthquakes. *Geology*, *37*(12), 1119–1122. https://doi.org/10.1130/G30143A.1

Abers, G. A., van Keken, P. E., & Hacker, B. R. (2017). The cold and relatively dry nature of mantle forearcs in subduction zones. *Nature Geoscience*, *10*(5), 333–337. https://doi.org/10.1038/ngeo2922

Audet, P., Bostock, M. G., Boyarko, D. C., Brudzinski, M. R., & Allen, R. M. (2010). Slab morphology in the Cascadia fore arc and its relation to episodic tremor and slip. *Journal of Geophysical Research*, *115*, B00A16. https://doi.org/10.1029/2008JB006053

Bedrosian, P. A., Peacock, J. R., Bowles-Martinez, E., Schultz, A., & Hill, G. J. (2018). Crustal inheritance and a top-down control on arc magmatism at Mount St Helens. *Nature Geoscience*, *11*(11), 865–870. https://doi.org/10.1038/s41561-018-0217-2

Blatter, D. L., Sisson, T. W., & Hankins, W. B. (2017). Voluminous arc dacites as amphibole reaction-boundary liquids. *Contributions to Mineralogy and Petrology*, *172*(5), 27. https://doi.org/10.1007/s00410-017-1340-6

Bostock, M. G. (2013). The Moho in subduction zones. *Tectonophysics*, *609*, 547–557. https://doi.org/10.1016/j.tecto.2012.07.007

Bostock, M. G., Hyndman, R. D., Rondenay, S., & Peacock, S. M. (2002). An inverted continental Moho and serpentinization of the forearc mantle. *Nature*, *417*(6888), 536–538. https://doi.org/10.1038/417536a

Bostock, M. G., & Rondenay, S. (1999). Migration of scattered teleseismic body waves. *Geophysical Journal International*, *137*(3), 732–746. https://doi.org/10.1046/j.1365-246x.1999.00813.x

Bostock, M. G., Rondenay, S., & Shragge, J. (2001). Multiparameter two-dimensional inversion of scattered teleseismic body waves 1. Theory for oblique incidence. *Journal of Geophysical Research*, *106*(B12), 30,771–30,782. https://doi.org/10.1029/2001JB000330

Brocher, T. M. (2005). Empirical relations between elastic wavespeeds and density in the Earth's crust. *Bulletin of the Seismological Society of America*, *95*(6), 2081–2092. https://doi.org/10.1785/0120050077

Brocher, T. M., Parsons, T., Tréhu, A. M., Snelson, C. M., & Fisher, M. A. (2003). Seismic evidence for widespread serpentinized forearc upper mantle along the Cascadia margin. *Geology*, *31*(3), 267–270. https://doi.org/10.1130/0091-7613(2003)031<0267:SEFWSF>2.0.CO;2

Cagnioncle, A.-M., Parmentier, E. M., & Elkins-Tanton, L. T. (2007). Effect of solid flow above a subducting slab on water distribution and melting at convergent plate boundaries. *Journal of Geophysical Research*, *112*, B09402. https://doi.org/10.1029/2007JB004934

Camp, V. E., & Ross, M. E. (2004). Mantle dynamics and genesis of mafic magmatism in the intermontane Pacific Northwest. *Journal of Geophysical Research*, *109*, B08204. https://doi.org/10.1029/2003JB002838

Crosbie, K. J. (2018). Shear velocity structure from ambient noise and teleseismic surface wave tomography in the Cascades around Mount St. Helens, MS Thesis, Cornell Univ.

Darold, A., & Humphreys, E. (2013). Upper mantle seismic structure beneath the Pacific Northwest: A plume-triggered delamination origin for the Columbia River flood basalt eruptions. *Earth and Planetary Science Letters*, *365*, 232–242. https://doi.org/10.1016/j.epsl.2013.01.024

Dueker, K. G., & Sheehan, A. F. (1997). Mantle discontinuity structure from midpoint stacks of converted P to S waves across the Yellowstone hotspot track. *Journal of Geophysical Research*, *102*(B4), 8313–8327. https://doi.org/10.1029/96JB03857

England, P., Engdahl, R., & Thatcher, W. (2004). Systematic variation in the depths of slabs beneath arc volcanoes. *Geophysical Journal International*, *156*(2), 377–408. https://doi.org/10.1111/j.1365-246X.2003.02132.x

England, P., & Wilkins, C. (2004). A simple analytical approximation to the temperature structure in subduction zones. *Geophysical Journal International*, *159*(3), 1138–1154. https://doi.org/10.1111/j.1365-246X.2004.02419.x

Evarts, R. C., Conrey, R. M., Fleck, R. J., Hagstrum, J. T. (2009). The Boring Volcanic Field of the Portland-Vancouver area, Oregon and Washington: Tectonically anomalous forearc volcanism in an urban setting. The Geological Society of America Field Guide #15, 253–270. https://doi.org/10.1130/2009.fld015(13)

Grove, T. L., Till, C. B., & Krawczynski, M. J. (2012). The role of H_2O in subduction zone magmatism. *Annual Review of Earth and Planetary Sciences*, *40*(1), 413–439. https://doi.org/10.1146/annurev-earth-042711-105310

Han, S., Carbotte, S. M., Canales, J. P., Nedimović, M. R., Carton, H., Gibson, J. C., & Horning, G. W. (2016). Seismic reflection imaging of the Juan de Fuca plate from ridge to trench: New constraints on the distribution of faulting and evolution of the crust prior to subduction. *Journal of Geophysical Research: Solid Earth*, *121*, 1849–1872. https://doi.org/10.1002/2015JB012416

Hansen, S. M., Schmandt, B., Levander, A., Kiser, E., Vidale, J. E., Abers, G. A., & Creager, K. C. (2016). Seismic evidence for a cold serpentinized mantle wedge beneath Mount St Helens. *Nature Communications*, *7*(1), 13242. https://doi.org/10.1038/ncomms13242

Hildreth, W. S. (2007). Quaternary Magmatism in the Cascades—Geological Perspectives. US Geological Survey Professional Paper 1744 (125 pp.).

Lee, C.-T. A., Luffi, P., Plank, T., Dalton, H., & Leeman, W. P. (2009). Constraints on the depths and temperatures of basaltic magma generation on Earth and other terrestrial planets using new thermobarometers for mafic magmas. *Earth and Planetary Science Letters*, *279*(1-2), 20–33. https://doi.org/10.1016/j.epsl.2008.12.020

Leeman, W. P., Lewis, J. F., Evarts, R. C., Conrey, R. M., & Streck, M. J. (2005). Petrologic constraints on the thermal structure of the Cascades arc. *Journal of Volcanology and Geothermal Research*, *140*(1-3), 67–105. https://doi.org/10.1016/j.jvolgeores.2004.07.016

McCrory, P. A., Blair, J. L., Waldhauser, F., & Oppenheimer, D. H. (2012). Juan de Fuca slab geometry and its relation to Wadati-Benioff zone seismicity. *Journal of Geophysical Research*, *117*, B09306. https://doi.org/10.1029/2012JB009407

McGary, R. S., Evans, R. L., Wannamaker, P. E., Elsenbeck, J., & Rondenay, S. (2014). Pathway from subducting slab to surface for melt and fluids beneath Mount Rainier. *Nature*, *511*(7509), 338–340. https://doi.org/10.1038/nature13493

Michaelson, C. A., & Weaver, C. S. (1986). Upper mantle structure from teleseismic P wave arrivals in Washington and northern Oregon. *Journal of Geophysical Research*, *91*(B2), 2077–2094. https://doi.org/10.1029/JB091iB02p02077

Nicholson, T., Bostock, M., & Cassidy, J. F. (2005). New constraints on subduction zone structure in northern Cascadia. *Geophysical Journal International*, *161*(3), 849–859. https://doi.org/10.1111/j.1365-246X.2005.02605.x

Obrebski, M., Allen, R. M., Xue, M., & Hung, S.-H. (2010). Slab-plume interaction beneath the Pacific Northwest. *Geophysical Research Letters*, *37*, L14305. https://doi.org/10.1029/2010GL043489

Parsons, T., Wells, R. E., Fisher, M. A., Flueh, E., & Ten Brink, U. S. (1999). Three-dimensional velocity structure of Siletzia and other accreted terranes in the Cascadia forearc of Washington. *Journal of Geophysical Research*, *104*(B8), 18,015–18,039. https://doi.org/10.1029/1999JB900106

Pearce, F. D., Rondenay, S., Sachpazi, M., Charalampakis, M., & Royden, L. H. (2012). Seismic investigation of the transition from continental to oceanic subduction along the western Hellenic Subduction Zone. *Journal of Geophysical Research*, *117*, B07306. https://doi.org/10.1029/2011JB009023

Reynard, B. (2013). Serpentine in active subduction zones. *Lithos*, *178*, 171–185. https://doi.org/10.1016/j.lithos.2012.10.012

Richards, P. G., Witte, D. C., & Ekström, G. (1991). Generalized ray theory for seismic waves in structures with planar nonparallel interfaces. *Bulletin of the Seismological Society of America*, *81*(4), 1309–1331.

Rondenay, S. (2009). Upper mantle imaging with array recordings of converted and scattered teleseismic waves. *Surveys in Geophysics*, *30*(4-5), 377–405. https://doi.org/10.1007/s10712-009-9071-5

Rondenay, S., Abers, G. A., & van Keken, P. E. (2008). Seismic imaging of subduction zone metamorphism. *Geology*, *36*(4), 275–278. https://doi.org/10.1130/G24112A.1

Rondenay, S., Bostock, M. G., & Shragge, J. (2001). Multiparameter two-dimensional inversion of scattered teleseismic body waves 3. Application to the Cascadia 1993 data set. *Journal of Geophysical Research*, *106*(B12), 30,795–30,807. https://doi.org/10.1029/2000JB000039

Ruscitto, D. M., Wallace, P. J., Johnson, E. R., Kent, A. J. R., & Bindeman, I. N. (2010). Volatile contents of mafic magmas from cinder cones in the Central Oregon High Cascades: Implications for magma formation and mantle conditions in a hot arc. *Earth and Planetary Science Letters*, *298*(1-2), 153–161. https://doi.org/10.1016/j.epsl.2010.07.037

Ryberg, T., & Weber, M. (2000). Receiver function arrays: A reflection seismic approach. *Geophysical Journal International*, *141*(1), 1–11. https://doi.org/10.1046/j.1365-246X.2000.00077.x

Syracuse, E. M., & Abers, G. A. (2006). Global compilation of variations in slab depth beneath arc volcanoes and implications. *Geochemistry, Geophysics, Geosystems*, *7*, Q05017. https://doi.org/10.1029/2005GC001045

Syracuse, E. M., van Keken, P. E., & Abers, G. A. (2010). The global range of subduction zone thermal models. *Physics of the Earth and Planetary Interiors*, *183*(1-2), 73–90. https://doi.org/10.1016/j.pepi.2010.02.004

van Keken, P. E., Hacker, B. R., Syracuse, E. M., & Abers, G. A. (2011). Subduction factory: 4. Depth-dependent flux of H_2O from subducting slabs worldwide. *Journal of Geophysical Research*, *116*, B01401. https://doi.org/10.1029/2010JB007922

van Keken, P. E., Wada, I., Abers, G. A., Hacker, B. R., & Wang, K. (2018). Mafic High-Pressure Rocks Are Preferentially Exhumed From Warm Subduction Settings. *Geochemistry, Geophysics, Geosystems*, *19*(9), 2934–2961. https://doi.org/10.1029/2018GC007624

Weaver, C. S., & Michaelson, C. A. (1985). Seismicity and volcanism in the Pacific Northwest: Evidence for the segmentation of the Juan De Fuca Plate. *Geophysical Research Letters*, *12*(4), 215–218. https://doi.org/10.1029/GL012i004p00215

Wells, R., Bukry, D., Friedman, R., Pyle, D., Duncan, R., Haeussler, P., & Wooden, J. (2014). Geologic history of Siletzia, a large igneous province in the Oregon and Washington Coast Range: Correlation to the geomagnetic polarity time scale and implications for a long-lived Yellowstone hotspot. *Geosphere*, *10*(4), 692–719. https://doi.org/10.1130/GES01018.1

Wilson, C. R., Spiegelman, M., van Keken, P. E., & Hacker, B. R. (2014). Fluid flow in subduction zones: The role of solid rheology and compaction pressure. *Earth and Planetary Science Letters*, *401*, 261–274. https://doi.org/10.1016/j.epsl.2014.05.052